We are IntechOpen,
the world's leading publisher of
Open Access books
Built by scientists, for scientists

6,900
Open access books available

185,000
International authors and editors

200M
Downloads

154
Countries delivered to

Our authors are among the

TOP 1%
most cited scientists

12.2%
Contributors from top 500 universities

CLARIVATE ANALYTICS
BOOK CITATION INDEX
INDEXED

WEB OF SCIENCE™

Selection of our books indexed in the Book Citation Index
in Web of Science™ Core Collection (BKCI)

Interested in publishing with us?
Contact book.department@intechopen.com

Ultrashort Extreme Ultraviolet Vortices

Laura Rego, Julio San Román, Luis Plaja,

Antonio Picón and Carlos Hernández-García

Additional information is available at the end of the chapter

Abstract

Optical vortices are very attractive because they transport a well-defined orbital angular momentum (OAM) associated with the singularity of the beam. These singular beams, commonly generated in the optical regime, are used in a wide range of applications: communication, micromanipulation, microscopy, among others. The production of OAM beams in the extreme ultraviolet (XUV) and X-ray regimes is of great interest as it allows to extend the applications of optical vortices down to the nanometric scale. Several proposals have been explored in order to generate XUV vortices in synchrotrons and FEL facilities. Here, we study the generation of XUV vortices through high-order harmonic generation (HHG). HHG is a unique source of coherent radiation extending from the XUV to the soft X-ray regime, emitted in the form of attosecond pulses. When driving HHG by OAM beams, highly charged XUV vortices with unprecedented spatiotemporal properties are emitted in the form of helical attosecond beams. In this chapter, we revise our theoretical work in the generation of XUV vortices by HHG. In particular, we illustrate in detail the role of macroscopic phase matching of high-order harmonics when driven by OAM beams, which allows to control the production of attosecond beams carrying OAM.

Keywords: high harmonic generation, attosecond pulses, orbital angular momentum, nonlinear optics, ultrafast phenomena, attosecond helical beams, extreme ultraviolet vortices, phase matching

1. Introduction

Light beams are known to carry spin angular momentum (SAM), related to their polarization, or orbital angular momentum (OAM), related to their spatial phase profile [1–3]. Helical phase beams, also called optical vortices, exhibit a transversal spiral phase structure around the beam

axis, thus having a well-defined OAM that is characterized by the topological charge, ℓ, i.e., the number of 2π-phase shifts along the azimuthal coordinate of the light beams. These beams are typically produced in the optical and infrared (IR) regimes, being used in a broad range of applications, such as optical communication [4, 5], micromanipulation [6, 7], and phase contrast microscopy [8, 9], among others [10]. There is a wide interest to bring helical phase beams into the extreme ultraviolet (XUV) and X-ray regimes, in order to extend their microscopy and spectroscopy applications down to the nanometric scale [11–17].

Schemes for the generation of helical phase beams in the XUV/X-ray regime have been reported in accelerator-based sources, such as synchrotrons and X-ray free-electron lasers (XFELs) [18–22], and in laser-based sources, such as plasma induced in solid surfaces [23, 24] or underdense plasmas [25] and high-order harmonic generation (HHG) in gas-phase media [16, 17, 26–30]. In general, accelerator-based sources produce more intense pulses but they are in the femto-second timescale (1 fs = 10^{-15} s) and their spatiotemporal coherence is not always ideal. On the other hand, laser-based sources produce shorter pulses, in the attosecond timescale (1 as = 10^{-18} s), with higher spatiotemporal coherence. In this chapter, we explore the unique properties of XUV vortices generated via HHG.

HHG is an extreme nonlinear process, driven in an atomic gas-phase medium interacting with an intense IR laser beam. This highly nonlinear interaction results in the emission of coherent harmonic radiation in the XUV and soft X-ray spectral regimes [31, 32]. The HHG radiation presents unique properties, the higher orders being emitted in the form of pulse trains at the attosecond timescale [33–37] or even at the zeptosecond scale if driven by mid-IR lasers [38]. Harmonics with well-defined OAM (OAM-HHG) can be generated using helical phase beams as driving fields. In such scenario, the phase twist is imprinted in the driving IR field—for which a single setup (diffractive mask, for instance) is required [39–41]—and is subsequently transferred to the short-wavelength radiation by nonlinear conversion. The first experiment of OAM-HHG [26] reported the generation of harmonic vortices with topological charge nearly equal to that of the fundamental field, i.e., the spiral phase structures of the harmonics and the fundamental driver beam are similar. Those experimental observations were attributed by the authors to nonlinear propagation effects and not to the OAM-HHG generation process itself. For instance, this finding was unexpected in terms of the present understanding of HHG, in which the harmonic phase scales roughly with the harmonic order [42]. Indeed, the spiral phase structure of the harmonics is expected to be that of the fundamental but multiplied by the harmonic order. In other words, if the driving OAM beam presents a topological charge ℓ, the qth-order harmonic should be emitted with a higher topological charge of $q\ell$. Shortly afterward, this expectation was demonstrated theoretically [27] and proven experimentally [16]. Interestingly, the highly-charged XUV vortices generated through HHG can by synthesized into helical attosecond beams [27–29]. Hence, HHG can be considered a direct route to generate XUV vortices, and nowadays, stands for a promising technique to produce very short (attosecond) vortices even in the soft X-ray regime.

Besides the promising applications of generating vortices in the XUV regime via HHG, there are still some fundamental questions that are very interesting to explore. High-harmonic radiation is a macroscopic output resulting from the emission of many atoms, but this

observable has its origin in a quantum mechanical (single-atom) mechanism and has indeed a strong correspondence, i.e., what occurs at the single-atom level in a particular spatiotemporal position will affect the macroscopic emission. OAM-HHG is indeed a clear example of this striking effect. Each atom in the target perceives a different transversal phase of the incoming IR field, and even though the atoms do not know the phases of their corresponding neighbors (they are not entangled), this information will be imprinted in the superposition of the photons emitted by the whole sample, giving rise to a transverse phase in the emitted radiation. This fascinating property raises questions such as how this process occurs and which are the significant mechanisms behind the imprinted (OAM) phase in the XUV harmonics. It is in fact a much unexplored field and more research is needed to understand the formation of XUV vortices via HHG.

In this chapter, we revise our theoretical work in the generation of XUV vortices by HHG. We provide a self-explanatory introduction of our theoretical models and we emphasize the most prominent results. In particular, we illustrate in detail the role of macroscopic phase matching of high-order harmonics when driven by OAM beams, leading to helical attosecond beams with unprecedented spatiotemporal properties.

The chapter is organized as follows. First, in Section 2 we introduce HHG, paying special attention to the semiclassical understanding of the process in terms of quantum paths. Second, in Section 3, we present the two theoretical methods that we have developed to simulate the HHG process driven by OAM beams. On one hand, we have developed advanced HHG simulations including quantum single-atom harmonic generation and macroscopic propagation. Our code, which is especially suited for beams without cylindrical symmetry, has been widely contrasted against experiments. On the other hand, we have further developed a simple semiclassical model that allows us to unveil the contribution from different quantum paths in the HHG process. This model is of special interest for the optical community using OAM-HHG, as it allows for qualitative description of future experiments. In Section 4, we present our results of OAM-HHG. We show the main properties (OAM content and divergence) of the generated XUV vortices. In addition, we analyze the phase-matching conditions of HHG driven by OAM, showing that different quantum path contributions to the HHG spectrum can be naturally selected by modifying the target position with respect to the driving beam focus. Finally, we analyze the properties of the temporal emission of the XUV vortices. In particular, we show that different XUV harmonic vortices can be synthesized to produce attosecond helical beams, whose spatiotemporal properties (such as divergence and/or temporal chirp) can be controlled through phase matching.

2. High-order harmonic generation

One of the major challenges since the invention of the laser [43] has been to extend coherent radiation to the extreme regions of the optical electromagnetic spectrum, and, in particular, to higher frequencies. For that purpose, harmonic generation offers a direct route. Although perturbative harmonics were obtained shortly afterwards the invention of the laser [44],

nonperturbative harmonics, i.e., those whose efficiency does not decrease exponentially with their order, were not reported until the late 1980s [45, 46]. At the very beginning, this behavior was attributed to multiphoton excitation of atomic subshells, but later, a nice classical interpretation was proposed, relating the harmonic generation with tunneling ionization in the so-called three-step model [47, 48]. Since then, the close interplay between theory and experiments has boosted the development of the field, providing a unique mechanism for the generation of extreme ultraviolet/soft X-ray radiation in the form of attosecond pulses [49–55].

HHG is achieved by focusing an intense femtosecond IR field into a gas target, as depicted in **Figure 1**. The target, either atomic or molecular, is commonly found in experiments as a gas jet, a gas cell, or a gas-filled capillary. The high nonlinear interaction between the IR field and each atom results in the emission of harmonics of the fundamental IR field, whose frequency extends into the XUV or even the soft X-ray regime. Notably, radiation emitted by the atoms is coherent. Hence, the harmonic signal reaching the detector is strongly affected by the phase matching of the high-order harmonics emitted by each atom of the target. Thus, HHG radiation results from the interplay between the microscopic single-atom emission and the macroscopic superposition of the contributions of all the atoms of the target.
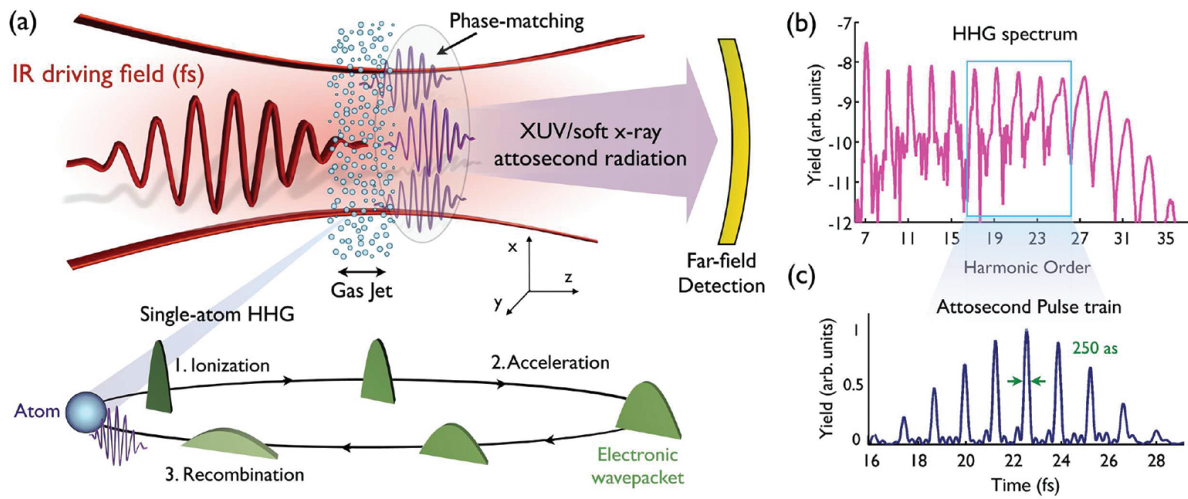

Figure 1. (a) (Top) Schematic view of a HHG experiment: an intense fs IR field is focused into a gas jet. Each atom interacting with the IR field emits XUV radiation in the form of higher-order harmonics. The harmonic signal at the detector is strongly affected by the phase matching of the radiation from all the emitters. At the bottom, we present a scheme of the single-atom HHG mechanism explained through the semiclassical three-step model: (i) ionization of the electronic wave packet through tunnel ionization; (ii) acceleration by the laser field; and (iii) recombination with the parent ion, resulting in the emission of higher-frequency radiation. (b) HHG spectrum obtained from a hydrogen atom driven by an 800 nm, 5.8 cycles (15 fs) FWHM, and 1.57×10^{14} W/cm^2 peak intensity laser pulse. The HHG spectrum is calculated with the quantum SFA+ theory in hydrogen (see Section 3.1). (c) Attosecond pulse train envelope obtained after performing the Fourier transform of the HHG spectrum presented in (b), windowed by a rectangular mask (blue) at the high-energy *plateau* region. Two attosecond pulses per cycle are obtained, of $\simeq$250 as FWHM pulse duration each one.

From the microscopic point of view, the single-atom HHG process is well described by the three-step model [47, 48], explained at the bottom of **Figure 1**: (i) an electronic wave packet is ionized by an intense laser via tunneling; (ii) once in the continuum, it is accelerated by the

field and driven back to the parent ion; and (iii) finally, upon recollision, it recombines, releasing high-frequency radiation whose energy corresponds to the kinetic energy acquired from the laser field plus the ionization potential. The dynamics of the electronic wave packet in the continuum can be described accurately using classical trajectories, from which it is simple to associate a particular recombination energy with an initial (ionization) time, as we will see in Section 2.2. Interestingly enough, for every half-cycle, there are two different electron paths leading to the same recombination energy, the so-called short and long trajectories. These short and long trajectories appear naturally as path contributions in the quantum framework within the strong-field approximation (SFA) [56, 57]. The phase of the HHG emission depends on the particular path followed by the electron, thus the interference of the emission from different paths may affect the structure of the harmonic spectrum. In addition, the time ordering of the short and long quantum paths gives rise to a positive or a negative chirp, respectively, in the temporal structure of the associated attosecond pulses [58]. We should also mention the possibility of longer quantum paths, evolving over more than a laser cycle, which give rise to higher-order rescatterings [59, 60] (providing zeptosecond waveforms in the high-order harmonic radiation driven by mid-IR pulses [38]). The HHG interferences from short and long quantum paths have been experimentally observed in standard HHG experiments [61]. In the OAM-HHG context, we started the first studies exploring the contributions of the different quantum paths to the harmonics, see Ref. [28]. In this chapter, we will revise the importance of the quantum paths in OAM-HHG.

Macroscopically, HHG in extensive targets can be intricate. Atoms located at different positions in the target emit harmonic radiation whose phase depends on the amplitude and phase of the local driving field. As a consequence, harmonic phase matching plays an essential role, limiting the spatial regions in which the harmonics contribute efficiently. Typically, harmonic phase matching is described in terms of the longitudinal coherence length that corresponds to the distance between two atoms whose emitted radiation interferes destructively, being a critical parameter for the optimization of HHG in macroscopic targets [62]. In addition, transverse phase matching is defined in terms of the transverse coherence length that describes the phase matching of the radiation coming from atoms placed in a plane perpendicular to the propagation axis [63]. Phase matching is essential to understand most of the macroscopic features of HHG radiation and to develop unique sources such as soft X-ray harmonics driven by mid-IR lasers [31]. Harmonic phase matching has been extensively studied in different macroscopic geometries, such as Gaussian beams focused into gas jets or gas cells [62, 64, 65] or transversal Bessel beams propagating in waveguides [66], among others. In Section 4.2, we discuss in detail some of the phase-matching properties of high-order harmonics driven by beams carrying OAM.

2.1. HHG radiation: XUV to soft X-ray radiation emitted in the form of attosecond pulses

Let us now analyze the main properties of the harmonic spectrum generated by an atom irradiated by an intense laser pulse. The harmonic spectrum presents certain peculiar features that have been observed since the earliest experiments and theoretical works [45, 46, 67, 68]. A typical HHG spectrum is composed of few, odd, low-order harmonics whose intensities

decrease exponentially, in accordance with the perturbative scaling, followed by a wide region of odd harmonics (the so-called *plateau*) with similar intensities. The *plateau* ends sharply at a cutoff frequency given by the law $\hbar\omega_{\text{cut-off}} \simeq I_p + 3.17 U_p$, where I_p is the ionization potential and U_p is the ponderomotive energy. The appearance of a *plateau* is a remarkable property, since it conveys the efficient emission of shorter wavelengths. Beyond the cutoff frequency, the intensity of the harmonics decreases again quickly and higher-order harmonics are hardly visible. The scaling of the harmonic q with the driving field intensity follows the law I^p, with $p < q$ at the *plateau* and cutoff regions, revealing their nonperturbative origins [69]. In **Figure 1(b)**, we present an example of an HHG spectrum. In particular, we show the simulated HHG spectrum obtained from the interaction of a hydrogen atom with a 800 nm, 5.8 cycles full width at half maximum (FWHM), and 1.57×10^{14} W/cm² peak intensity laser pulse.

There is a fundamental interest in extending the cutoff frequency to higher energies. From the dependences of the ponderomotive energy, $U_p \propto \lambda_0^2 I$, and the cutoff law, the HHG spectrum can be extended toward higher energies by increasing the intensity (I) or/and the wavelength (λ_0) of the driving field. However, there are physical restrictions that limit the maximum photon energy of the harmonic spectra. First, if we increase the laser intensity beyond a critical point, we move to the barrier-suppression regime for ionization, where the spectral *plateau* is degraded [70]. Second, the efficiency for the generation of the highest harmonic orders has been shown to decrease drastically with the driving wavelength [59, 71]. In addition, phase-matching conditions may decrease the efficiency of the harmonics when both increasing the intensity and the wavelength of the driving laser field. Nevertheless, recently, it has been possible to define experimental conditions in which favorable phase matching is naturally achieved, leading to the efficient emission of soft X-ray HHG radiation, if driven by mid-IR [31], or vacuum ultraviolet fields [32].

On the other hand, HHG offers the exciting perspective of synthesizing XUV pulses of attosecond duration [33, 34]. An attosecond pulse train is obtained by the selection of the higher frequency part of the HHG spectrum, i.e., the *plateau*. This synthesis is possible because the *plateau* is composed of harmonics with similar intensities (like a frequency comb) and phases [33]. In **Figure 1(c)**, we present the attosecond pulse train envelope computed from the inverse Fourier transform of the complex harmonic spectrum presented in **Figure 1(b)**, windowed by a rectangular mask (blue) of ten photons bandwidth ($10\omega_0$, where ω_0 is the fundamental frequency) at the high-energy *plateau*. An attosecond pulse is emitted in each half-cycle of the incident laser pulse. Note that the obtention of odd-order harmonics results from the integration of attosecond pulses delayed by half a cycle, and with an overall phase shift of π, coming from the sign of the driving field.

The first experimental measurement of an attosecond pulse train was performed by selecting five consecutive harmonics generated in argon, obtaining 250 as pulses [35]. In addition, isolated pulses with duration of 650 as were produced by spectrally filtering few cutoff harmonics produced by an ultrashort laser pulse [36]. At present, after postcompression, isolated pulses with temporal durations < 100 attoseconds have been measured experimen-

tally [37, 72]. Moreover, there is a great interest to extend the production of isolated attosecond pulses to the soft X-ray regime [73, 74], and there are proposals to produce subattosecond waveforms by using mid-IR driving pulses [38].

2.2. Quantum path contributions to HHG

A beautifully simple picture to understand the single-atom HHG process is given by the three-step model [47, 48], based on the so-called simple man's model. In the tunneling regime, one can assume that the ionization process depends only on the instantaneous value of the electromagnetic field, and right after ionization, the electron is located at the coordinate origin with zero velocity. Another assumption of this model consists in considering the dynamics subsequent to ionization as corresponding to a classical free electron in the electromagnetic field, thus neglecting the influence of the Coulomb potential. As a consequence, HHG can be understood in terms of simple semiclassical arguments, as explained at the bottom of **Figure 1(a)**.

We can study in detail the electronic dynamics in the three-step model by integrating the classical equations of motion given by Newton's law and using the conditions given by the simple man's model. In **Figure 2(a)**, we have depicted some electron trajectories for different ionization times, in the presence of a monochromatic laser field of $\lambda_0 = 800$ nm and peak intensity of 1.57×10^{14} W/cm². The gray-dashed line represents the electric field in arbitrary units, whereas the green line represents the nucleus position, located at the coordinate origin. Note that we have represented some of the trajectories that lead to recollision, as those that do not recollide will not contribute to the HHG process. In **Figure 2(b)**, we have plotted the recollision kinetic energy of the particles as a function of the recollision (green points) and ionization (red points) times. Note that there is one particular trajectory, represented in blue, whose recollision energy is maximum, taking the well-known value of $3.17U_p$. This trajectory leads to the emission of the cutoff energy, and presents an excursion time of approximately 0.63 times the period of the laser pulse. Further recollisions do not raise this maximum energy. Noticeably, in every half-cycle of the laser pulse, there are two possible electron trajectories leading to the same kinetic energy at recollision and therefore two possible paths for the generation of the same harmonic (each named accordingly to the excursion time as *short* and *long* trajectories). We have represented in **Figure 2(a)** three pairs of short and long trajectories with energies at recollision of $3.0U_p$ (purple), $2.5U_p$ (dark pink), and $1.5U_p$ (light pink).

The short and long path contributions also emerge from the quantum framework within the strong-field approximation [56, 57, 75]. The phase of the harmonic emission not only depends on the phase of the fundamental field but also on the particular path followed by the electron. This additional nonperturbative term, the so-called *intrinsic* phase, is proportional to the ponderomotive potential times the excursion time of the quantum path [75]. As a consequence, the structure of the HHG spectrum may be intricate, as it results from the interference of the emissions of the different quantum paths [61]. In addition, since the different electronic trajectories rescatter at different times (see **Figure 2**), a chirp is imprinted in the emitted radiation [58, 76, 77]. The emission from the short trajectories is positively chirped, i.e., the

lower harmonics are emitted before the higher, as depicted by the positive slope of the green curve in **Figure 2(b)**. On the other hand, the emission from the long trajectories exhibits a negative chirp, as depicted by the negative slope of the green curve in **Figure 2(b)**. As a result, the HHG mechanism itself prevents the harmonics to be emitted in the Fourier limit.
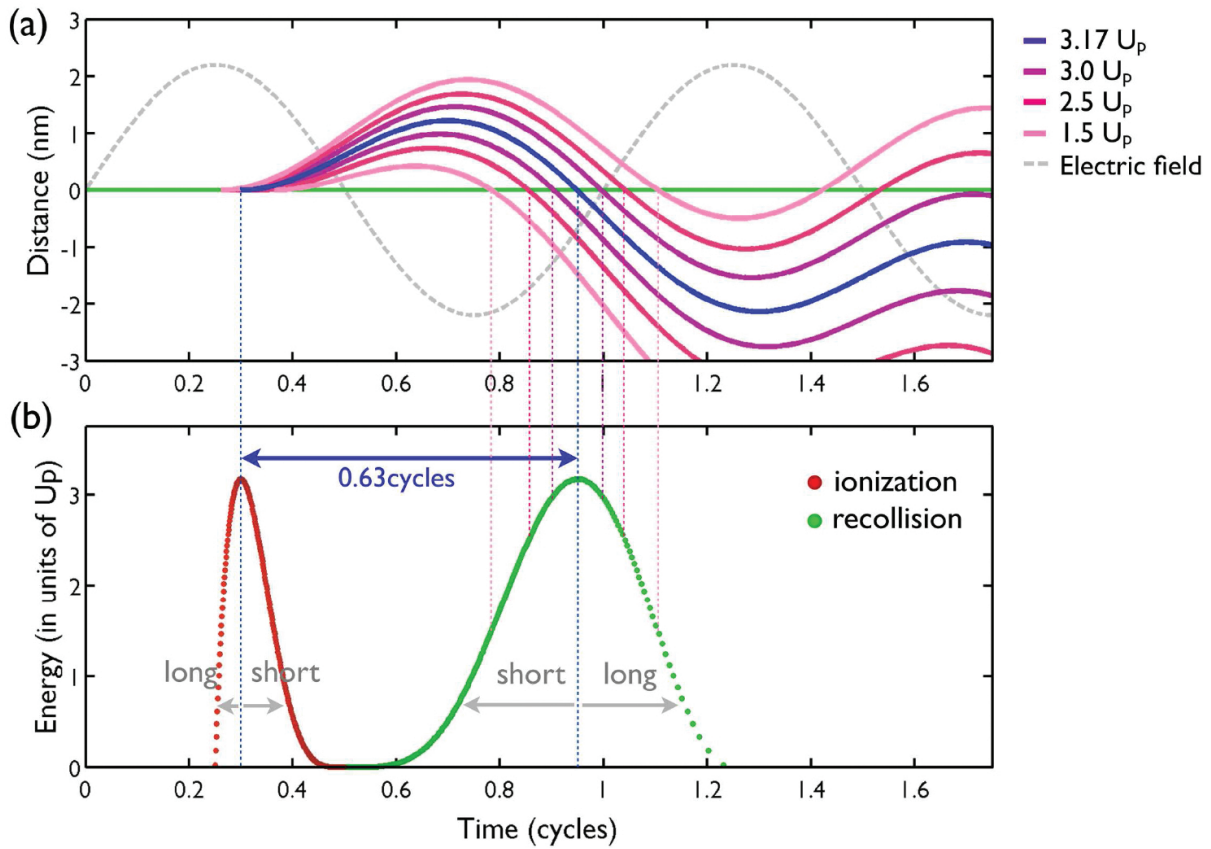

Figure 2. (a) Sample of electronic trajectories in a monochromatic laser field of λ_0 = 800 nm and peak intensity of 1.57×10^{14} W/cm². The gray-dashed line represents the electric field (arb. units), whereas the green line, the nucleus position. Three pairs of short and long trajectories are represented for energies at recollision of $3.0 U_p$ (purple), $2.5 U_p$ (dark pink), and $1.5 U_p$ (light pink), whereas the most energetic trajectory, raising 3.17_p at recollision, is represented in blue. The vertical axis represents the distance from the nucleus. (b) Returning kinetic energy of the electrons at the instant of the first recollision in (a). The green points represent the recollision time, whereas the red points, the ionization time.

3. Theoretical treatment of OAM-HHG

The theoretical treatment of HHG admits different levels of description, ranging from the classical to semiclassical and full quantum. For instance, in the previous section, we have shown how HHG can be studied through classical electron trajectories. In this section, we build a theoretical model to describe HHG driven by OAM beams, which takes into account both microscopic and macroscopic physics. We have developed two alternative, full quantum and semiclassical, methods that allow us to describe and have an insight into the microscopic quantum paths involved in the formation of OAM vortices.

Let's start putting in context the physical scenario of HHG driven by OAM beams. In **Figure 3**, we present an schematic view of OAM-HHG. A pulsed vortex beam centered at $\lambda_0 = 800$ nm, a typical wavelength used for HHG, is focused into a gas jet. In this work, we use an argon gas, and the amplitude of the field E_0 is chosen to give a peak intensity of 1.4×10^{14} W/cm² at the focus. High-order harmonics are emitted at each atom in the target, and, upon propagation, their coherent addition results in the far-field emission of XUV vortices, represented along the divergence β and azimuth φ coordinates.

The spatial structure of the IR vortex beam is represented by a monochromatic Laguerre-Gaussian beam propagating in the z-direction, with wavelength $\lambda_0(k_0 = 2\pi/\lambda_0)$ expressed as $LG_{\ell,p}(r,\phi,z;k_0)e^{ik_0z}$, where

$$LG_{\ell,p}(r,\phi,z;k_0) = E_0 \frac{w_0}{w(z)}\left(\frac{\sqrt{2}r}{w(z)}\right)^{|\ell|} L_p^{|\ell|}\left(\frac{2r^2}{w^2(z)}\right)\exp\left(-\frac{r^2}{w^2(z)}\right)\exp\left[i\ell\phi + i\frac{k_0 r^2}{2R(z)} + i\Phi_G(z)\right], \qquad (1)$$

and $w(z) = w_0\sqrt{1 + (z/z_0)^2}$, with w_0 being the waist of the mode, $z_0 = k_0 w_0^2/2$ the Rayleigh range, $R(z) = z\left[1 + (z_0/z)^2\right]$ the phase-front radius, $\Phi_\ell(z) = -(2p + |\ell| + 1)\arctan(z/z_0)$ the Gouy phase, and $L_p^{|\ell|}(x)$ the associated Laguerre polynomials
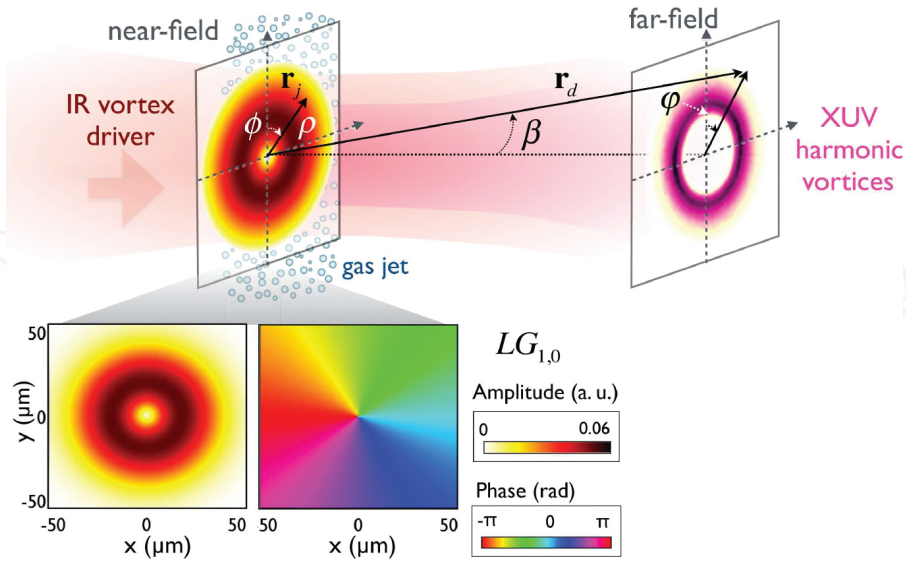

Figure 3. Scheme of HHG driven by OAM beams. An intense IR vortex beam carrying OAM (with $\ell = 1$ in this case) is focused into an argon gas jet. The near-field coordinates are (ρ,ϕ). Each atom emits HHG radiation that, upon propagation, results in the far-field emission of XUV vortices with some divergence and azimuth (β,φ). In the bottom, we show the near-field amplitude (left) and phase (right) of the $LG_{1,0}$ IR mode, with beam waist of 30 μm.

$$L_p^{|\ell|}(x) = \sum_{m=0}^{p} (-1)^m \frac{(|\ell|+p)!}{(p-m)!(|\ell|+m)!m!} x^m. \tag{2}$$

The indices $\ell = 0, \pm 1, \pm 2,...$ and $p = 0,1,2,...$ correspond to the topological charge and the number of nonaxial radial nodes of the mode, respectively. At the bottom of **Figure 3**, we present the amplitude (left) and phase (right) of the $LG_{1,0}$ IR mode. In the simulations presented in this work, we have considered a well-defined OAM of $\ell = 1$ and $p = 0$ as a driving field, with a beam waist of $w_0 = 30$ μm and, therefore, a Rayleigh range of $z_0 = 3.5$ mm.

3.1. 3D quantum SFA theory

We have developed a quantum method to compute HHG including both single-atom (micro-scopic) and phase matching (macroscopic) physics. In order to take into account macroscopic phase matching, we compute harmonic propagation using the electromagnetic field propaga-tor [78]. To this end, we discretize the target (gas jet) into a set of j elementary radiating volumes (typically $> 10^5$), as sketched in **Figure 3**, and propagate the emitted field $\mathbf{E}_j(\mathbf{r}_j, t)$ to the far-field detector,

$$\mathbf{E}_j(\mathbf{r}_d, t) = \frac{q_j \mathbf{s}_d}{c^2 |\mathbf{r}_d - \mathbf{r}_j|} \times \left[\mathbf{s}_d \times \mathbf{a}_j \left(t - \frac{|\mathbf{r}_d - \mathbf{r}_j|}{c} \right) \right] \tag{3}$$

where s_d is the unitary vector pointing to the detector, $\mathbf{r}_d$ and $\mathbf{r}_j$ are the position vectors of the far-field detector and of the near-field elementary radiator j, respectively, and $\mathbf{a}_j$ is the dipole acceleration of each elementary source. Note that in Eq. (3), the harmonic radiation is assumed to propagate with the vacuum phase velocity, which is a reasonable assumption for high-order harmonics. The harmonic field reaching the detector is thus calculated as the coherent addition of these elementary contributions. Propagation effects in the driving field, such as the pro-duction of plasma, the refractive index of the neutrals, the group-velocity walkoff [79], as well as the absorption in the propagation of the harmonics are also taken into account.

In the case of intense fields, the computation of the microscopic HHG dynamics of the elementary radiators is not trivial, as the interaction is nonperturbative. Due to the large number of radiators, the use of exact numerical integration of the time-dependent Schrödinger equation becomes extremely expensive. Therefore, the use of simplified models is almost mandatory. In the case of intense fields, S-matrix approaches combined with the strong-field approximation [80–82] are demonstrated to retain most of the features of the HHG process [75, 83]. We use an extension of the standard SFA, hence we will refer it as SFA+, where the total dipole acceleration of the j radiator ($\mathbf{a}_j$) is found from two contributions, a_b and a_d, the first being the standard SFA expression and the latter being a correction due to the instantaneous dressing of the ground state. This method computes the dipole acceleration directly from the superposition of the contributions of each Volkov wave, each can be integrated separately as

an ordinary 1D equation, leading to a very efficient algorithm [71, 84]. The single-atom HHG spectrum can be found after performing the Fourier transform of the dipole acceleration.

One of the advantages of this method, which takes into account both microscopic and macroscopic HHG, is that it is well-fitted to nonsymmetric geometries, therefore, it is especially suited for computing HHG driven by singular beams, such as those carrying OAM. The method has been successfully used for describing regular HHG with near- and mid-IR lasers, in good agreement with several experiments [31, 63, 73, 85–88].

For the simulation results presented in this work, we have considered a laser pulse with a well-defined OAM of $\ell = 1$ as a driving field. The laser pulse is assumed to have a temporal envelope of $\sin^2(\pi t / NT)$, where N=16 cycles and T is the laser period (2.67 fs). The FWHM of the pulse is 15.4 fs and the peak intensity is 1.4×10^{14} W/cm². The detector is assumed to be far enough from the interaction area in order to comply with the far-field condition. The target is an argon gas jet, directed along the x-axis, and modeled by a Gaussian distribution along the y and z dimensions (whose FWHM is 500 μm), and a constant profile along its axial dimension, x. The peak density is 10^{17} atoms/cm³.

3.2. The thin slab model (TSM)

We have developed a simple model, the *thin slab model* (referred as quantum path OAM model in [28]), to gain insight on the physical origin of the structure of the XUV vortices generated via HHG. In this simplified description, the target is represented by a thin (2D) slab placed perpendicular to the propagation axis of the fundamental beam. As a consequence, our approach does not take into account longitudinal phase matching, allowing us to focus the discussion on transverse phase matching [63] that is expected to be relevant due to the transverse structure of OAM beams.

The complex beam profile of the fundamental field in the thin slab, placed at a propagation distance z_t, can be written as

$$A(r) = U(\rho, \phi, z_t) e^{i\Phi(\rho, \phi, z_t)},$$

(4)

where $\Phi(\mathbf{r})$ contains the phase terms presented in the exponential of Eq. (1) and the amplitude terms are grouped in $U(\mathbf{r})$.

We consider the high-order harmonics to be emitted at the thin slab. Let us see how their intensity and phase profiles are related to that of the driving field. In the perturbative regime, the amplitude of the qth harmonic is proportional to the power of the fundamental beam amplitude $\propto U(\mathbf{r})^q$. However, since HHG is highly nonperturbative, the amplitude of the generated harmonic scales with a lower power [69]. As a consequence, the harmonic field at the slab can be approximated by an analytic SFA representation, first used in [42]. This representation gives a different scaling of the amplitude and harmonic phase with the driving

field. First, the amplitude of the qth harmonic is proportional to the pth power of the fundamental amplitude $U(\mathbf{r})^p$, where $p < q$ reflects the nonperturbative HHG behavior, being approximately constant for the harmonics in the *plateau* region. In order to extract the value of the p exponent, and thus the scaling of the harmonic amplitude with the driving field, we perform single-atom HHG calculations using the SFA+ approach. We present in **Figure 4(a)**, the HHG spectra (log scale) driven by an 800 nm laser field for three different peak intensities. The driving laser pulse is assumed to have a temporal envelope of $\sin^2(\pi t/NT)$, where $N = 64$ cycles and T is the laser period (2.67 fs). The FWHM of the pulse is 61.4 fs. The amplitude of the field is chosen to give peak intensities of 0.875×10^{14} W/cm² (red), 1.177×10^{14} W/cm² (green), and 1.524×10^{14} W/cm² (blue). In **Figure 4(b)–(e)**, we show the scaling for the peak of the 17th, 19th, 21st, and 23rd harmonics, respectively, with the driving field amplitude (log scale). The oscillations of the harmonic peak amplitudes with the driving amplitude are a known consequence of the interference between the short and long quantum path contributions [61]. By performing a linear fit out of the logarithmic plot, we extract the p exponent, being 3.7, 3.9, 3.4, and 3.6 for the 17th, 19th, 21st, and 23rd harmonics, respectively. As commented above, the value obtained for p is very similar for the harmonics in the *plateau* region of the spectrum.
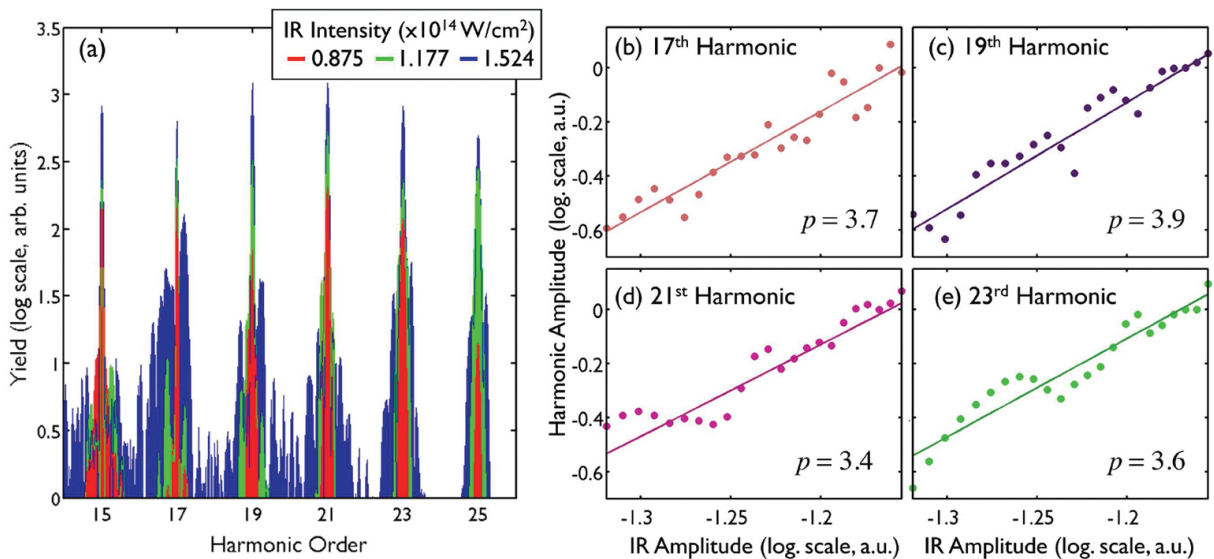

Figure 4. Scaling of the harmonic amplitude with the driver field. (a) Single-atom HHG spectrum (log scale) calculated using the SFA+ approach, driven by a 800 nm laser pulse modeled by a $\sin^2$ envelope with 61.4 fs FWHM, and peak intensities of 0.875×10^{14} W/cm² (red), 1.117×10^{14} W/cm² (green), and 1.524×10^{14} W/cm² (blue). The scaling of the 17th (b), 19th (c), 21st (d), and 23rd (e) harmonics with the driver amplitude is fitted to a power p of 3.7, 3.9, 3.4, and 3.6, respectively.

On the other hand, the phase of the harmonics scales with q times the phase of the driving field $q\Phi(\mathbf{r})$, and has an additional nonperturbative term, the *intrinsic* phase, which is proportional to the intensity of the fundamental field $\alpha_q^j |U(\mathbf{r})|^2$. The strong-field parameters α_q^j

depend on the electronic quantum path (j) (short or long) followed by the semiclassical description of the HHG process (see Section 2.2). They can be calculated from the action of classical trajectories with recollision energies leading to the considered harmonic [62]. For the simulations considered in this chapter, the strong-field parameters for the 19th harmonic for the short (S) and long (L) quantum path contributions are found to be $\alpha_{19}^S = 2.75 \times 10^{-14}$ cm^2 W^{-1} and $\alpha_{19}^L = 2.220 \times 10^{-13}$ cm^2 W^{-1}.

Taking into account the previous arguments for the description of the high-order harmonics in the analytic SFA representation, the contribution of the j quantum path (short or long) to the qth harmonic emitted at a slab located at z_t can be written as

$$A_q^j(\rho,\phi,z_t) = \left(\frac{C}{\tau^j}\right)^{3/2} |U(\rho,\phi,z_t)|^p \, e^{iq\Phi(\rho,\phi,z_t)} e^{i\alpha_q^j |U(\rho,\phi,z_t)|^2} \tag{5}$$

where C is a constant and τ^j is the excursion time associated with the j quantum path [75], affecting the efficiency of HHG due to the quantum diffusion of the electron wave packet.

Once we have the description of the qth harmonic field at the slab, we use Fraunhofer diffraction theory to calculate the far-field signal. The qth harmonic field at the divergence β and azimuthal ϕ coordinates is given by the Fraunhofer integral

$$F_q^j(\beta,\varphi) \propto \int_0^\infty \int_0^{2\pi} \rho' d\rho' d\phi' A_q^j(\mathbf{r}') e^{-i\frac{2\pi}{\lambda_q}\rho' \tan\beta \cos(\varphi-\phi')} , \tag{6}$$

$$F_q^j(\beta,\varphi) \propto \left(\frac{C}{\tau^j}\right)^{3/2} \int_0^\infty \int_0^{2\pi} \rho' d\rho' d\phi' |U(\rho',\phi',z_t)|^p \, e^{iq\Phi(\rho',\phi',z_t)} e^{i\alpha_q^j |U(\rho',\phi',z_t)|^2} e^{-i\frac{2\pi}{\lambda_q}\rho' \tan\beta \cos(\varphi-\phi')} \tag{7}$$

where (ρ',φ') represents the near-field polar coordinates and λ_q is the wavelength of the qth harmonic related to the fundamental wavelength as $\lambda_q = \lambda_0/q$. Now, using (5), we obtain

While this equation is valid for a driving field composed of any combination of Laguerre-Gaussian modes, let us now consider a driving field composed of a single OAM mode. In this case, the intensity of the driving does not vary along the azimuthal coordinate, i.e., $|U(\rho',\varphi', z_t)| = |U(\rho',z_t)|$, and we can perform the analytic integral over φ'. By considering the phase part of the fundamental Laguerre-Gaussian beam in Eq. (1), we finally obtain a compact formula that includes the dependence on both the fundamental OAM (ℓ) and the quantum path contribution (j) [28],

$$F_q^j(\beta) \propto \left(\frac{C}{\tau^j}\right)^{3/2} \int \rho' d\rho' \, |U(\rho', z_t)|^p \, e^{iq\frac{k_0\rho'^2}{2R(z_t)}} e^{iq\Phi_G(z_t)} e^{i\alpha_q^j|U(\rho', z_t)|^2} J_{q\ell}\left(\frac{2\pi}{\lambda_q}\beta\rho'\right). \tag{8}$$

Note that the detected harmonic signal will result from the superposition of short and long quantum path contributions. We remark that Eq. (8) is valid when the fundamental beam is composed by a single OAM mode. For any combination of different OAM modes, one should use Eq. (7) [30].

4. Results: XUV harmonic vortices

Once we have introduced the theoretical methods, we can proceed with the discussion of the main results of OAM-HHG. First, in Section 4.1, we describe the main properties of the XUV vortices that are generated. We will concentrate on their OAM content and divergence. Second, in subsection 4.2, we will analyze how macroscopic phase-matching conditions affect the process of OAM-HHG. We will observe how short and long quantum path contributions can be naturally isolated by adjusting the relative position between the gas jet and the driving beam focus. Finally, in Section 4.3, we will describe the rich spatiotemporal structure of the helical attosecond beams that emerges when several XUV vortices are synthesized.

4.1. XUV vortices: OAM content and divergence

Let us now investigate the main properties of the XUV vortices generated via HHG. In **Figure 5**, we present the intensity (top) and phase (bottom) far-field angular profiles of the 17th (a), 19th (b), 21st (c), and 23rd (d) harmonic vortices. These results are obtained using the 3D quantum SFA simulations, where we have placed the argon jet at the focus position of the $LG_{1,0}$ mode shown in **Figure 3**. Two main conclusions arise from these plots. First, the radius of the annular intensity distribution is similar for all the harmonics, and thus, they are emitted with similar divergence. Note that some of the harmonics exhibit secondary rings due to phase matching, as we discuss in detail in subsection 4.2. Second, the phase-plots show that the topological charge of the qth-order harmonic is q, leading to a simple scaling of the topological charge with the harmonic order $\ell_q = q\ell$ (ℓ_q being the topological charge of the qth harmonic). This scaling of OAM in HHG was first predicted theoretically in Ref. [27] and later confirmed experimentally in Ref. [16]. Note that this simple selection rule follows the energy conservation law for the harmonic conversion process $\omega_q = q\omega$ (ω being the frequency of the fundamental field), which was previously found in perturbative OAM harmonic generation [89–92]. However, this simple rule may result unexpected in the nonperturbative regime, since the intrinsic phase is not directly related to a specific multiphoton channel. Recently, we have shown that the nonperturbative nature of HHG modifies the selection rule for the OAM build-up only if the driving beam is composed of different $LG_{\ell,p}$ modes [30]. If pure OAM modes are used, the OAM build-up in HHG is thus governed by the simple selection rule $\ell_q = q\ell$.
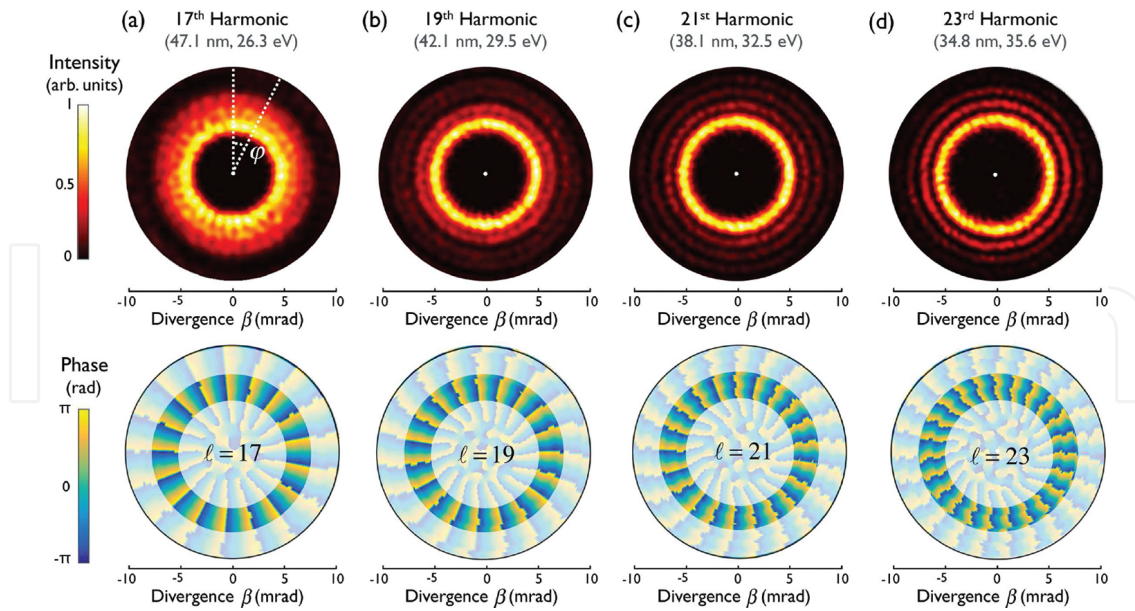
Figure 5. Intensity (top) and phase (bottom) far-field angular profiles of the 17th (a), 19th (b), 21st (c), and 23th (d) harmonics, obtained with the 3D quantum SFA simulations. The argon gas jet is placed at the focus of a $LG_{1,0}$ mode, with a beam waist of $w_0 = 30$ μm and $\lambda_0 = 800$ nm. The amplitude is chosen to give a peak intensity of 1.14×10^{14} W/cm^2 at the focus. Note that the resulting topological charge (obtained from the phase plots) follows the scaling law $l_q = ql$ and thus, resulting in $l_{17} = 17$ to $l_{23} = 23$.

It is interesting to note that in the OAM-HHG experiments [16, 26, 29] and theoretical works [27, 28] performed to date, the divergence of all the harmonics was found to be similar, in contrast to standard HHG driven by Gaussian beams, where the divergence decreases with the harmonic order. In fact, this result is a consequence of the OAM build-up law $\ell_q = q\ell$ [29].

We can disentangle it from the final expression of our TSM approach, given by Eq. (8). The dependence on the divergence in the TSM appears in the Bessel function, which is a part of the amplitude of the integrand of the equation. The order of this Bessel function is directly related to the OAM of the qth harmonic generated in the process $q\ell$. The argument, which is proportional to the divergence, is inversely proportional to the wavelength of the qth harmonic λ_q. Consequently, both, the order and the argument of the Bessel function, are proportional to the harmonic order q, which is the reason why the position of the maximum of the amplitude of the integrand of Eq. (8) is almost invariant with respect to the harmonic order. To prove this similarity, we show in **Figure 6** this amplitude as a function of the divergence for different harmonic orders [19th (blue), 21st (green), 23rd (red), 25th (cyan), and 27th (purple)]. The amplitudes have been calculated at the radius at which the function $rU^p(r,z_t = 0)$ takes the maximum value. As it can be observed, the signal of all the harmonics rises around $\beta \simeq 6$ mrad, where all of them present a maximum amplitude.

HHG leads to a perfect vortex generation process in terms of its applicability [93], as all these XUV vortices of topological charge $q\ell$ are emitted with similar size. First, HHG offers a unique possibility to generate energy-tunable OAM beams, by selecting different harmonic orders (for example, in **Figure 5**, from 26.3 to 35.6 eV), which, in principle, could be extended to the soft X-ray regime if mid-IR drivers were used [31]. Second, HHG provides a unique tool to produce

OAM-tunable XUV vortices, by directly changing the topological charge of the driving beam ℓ, or, for example, by using a crossed beam geometry, where the noncollinear beams present different OAM and wavelength properties [16]. Recently, the use of driving beams carrying a superposition of different OAM contributions revealed a rich scenario in which XUV vortices present multiple OAM contributions arising from the nonperturbative behavior of HHG [30], offering a new route to generate OAM-tunable vortex beams.
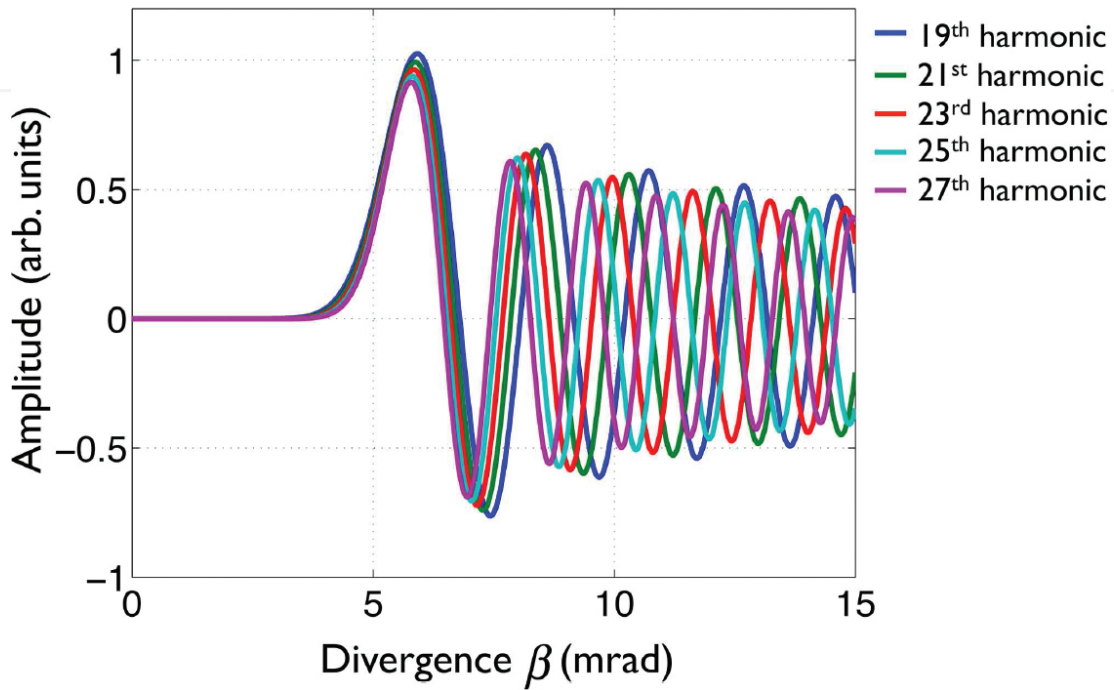
Figure 6. Amplitude of the integrand of Eq. (8), $r_0 U^p(r_0, z_t = 0) J_{q\ell}(2\pi\beta r_0/\lambda_q)$, for different harmonic orders (q going from 19th to 27th), and r_0 being the radius where we obtain the maximum of the function $r U^p(r, z_t = 0)$. The divergence where the integrand is maximized is very similar for all harmonic orders ($\beta \simeq 6$ mrad). Note that in the order of the Bessel function, we have considered the OAM build-up law, $\ell_q = q\ell$, which appears to be a necessary condition for emitting XUV harmonic vortices with similar divergences.

4.2. Phase-matching effects in OAM-HHG

Once we have presented the main properties of the XUV vortices generated via HHG (divergence and OAM content), we study the effect of macroscopic phase matching on their generation. Harmonic phase-matching conditions are known to depend strongly on the position of the target with respect to the focus of the driving field [62]. In particular, in standard HHG experiments with Gaussian beams, short quantum path contributions dominate the detected HHG emission if the gas target is placed after the focus position. However, if the target is placed before the focus, long quantum paths dominate for low divergence angles while the short ones dominate at larger angles [64, 65]. In this section, we discuss the effects of the relative position between the target and the beam focus in HHG driven by helical-phase beams carrying OAM. First, we make use of our TSM approach to disentangle the short and long quantum path

contributions under different phase-matching conditions. Second, we perform a time-frequency analysis (TFA) to identify the quantum path contributions in the 3D quantum SFA simulations. More information about the phase matching in OAM-HHG can be found in Ref. [28].

4.2.1. Disentangling quantum path contributions with the thin slab model

In **Figure 7**, we show the intensity profile (log scale) of the 19th harmonic as a function of the target position along the propagation distance. To this end, the intensity angular profile along the divergence β for a fixed azimuth $\varphi = 0$ is shown as a function of the target position z_t, where $z_t < 0$ ($z_t > 0$) stands for a target placed before (after) the focus position. Note that the horizontal axis can be read as the radial axis of the emitted OAM ring. First, we show in panel (a), the results obtained with the 3D quantum SFA model, where we have considered the target as a thin slab of 1 μm. We observe that both the divergence and the thickness of the harmonic vortex ring vary substantially with respect to the slab position. Moreover, in addition to the main intensity structure emitted at 5–6 mrad, we observe additional structures with larger divergence if $z_t > 0$ and with lower divergence if $z_t < 0$.
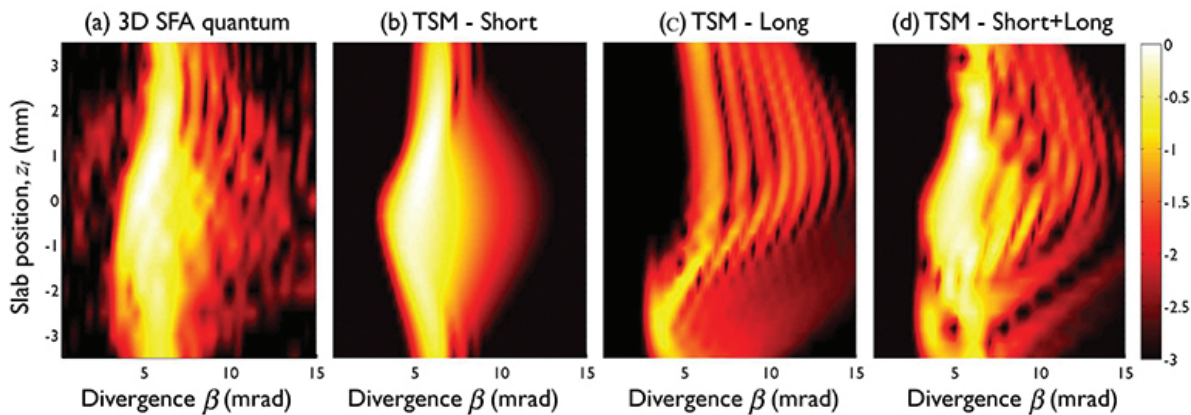

Figure 7. Angular dependence of the 19th harmonic as a function of the slab position z_t. Panel (a) shows the result obtained from the full 3D quantum SFA model. Panels (b–d) are obtained from the TSM, using the same parameters as in (a), but considering the short quantum paths (b), the long ones (c) and the coherent addition of both of them (d).

In order to get a qualitative explanation of the divergence profiles observed in panel (a) of **Figure 7**, we use the *thin slab model*. To this end, we calculate the 19th harmonic far-field signal by integrating Eq. (8) with the same beam parameters as used in panel (a), where the pth power of the harmonic amplitude is $p = 3.9$ and the strong-field parameters are $\alpha_{19}^S = 2.75 \times 10^{-14}$ cm²/W and $\alpha_{19}^L = 2.220 \times 10^{-13}$ cm²/W. We can separately obtain the harmonic contributions from different quantum paths with the TSM. Thus, we present the intensity profile of the short (b), long (c) and short + long (d) quantum path contributions to the 19th harmonic as a function of z_t. Note that in panel (d), short and long contributions are added coherently taking

into account the semiclassical excursion times [see Eq. (8)]. The excellent agreement between the 3D SFA quantum simulations in panel (a) and the short + long TSM results in panel (d) serves as a validation of the TSM. As a result, we can use the results in panels (b) and (c) to identify the main features of panel (a) in terms of short and long quantum paths.
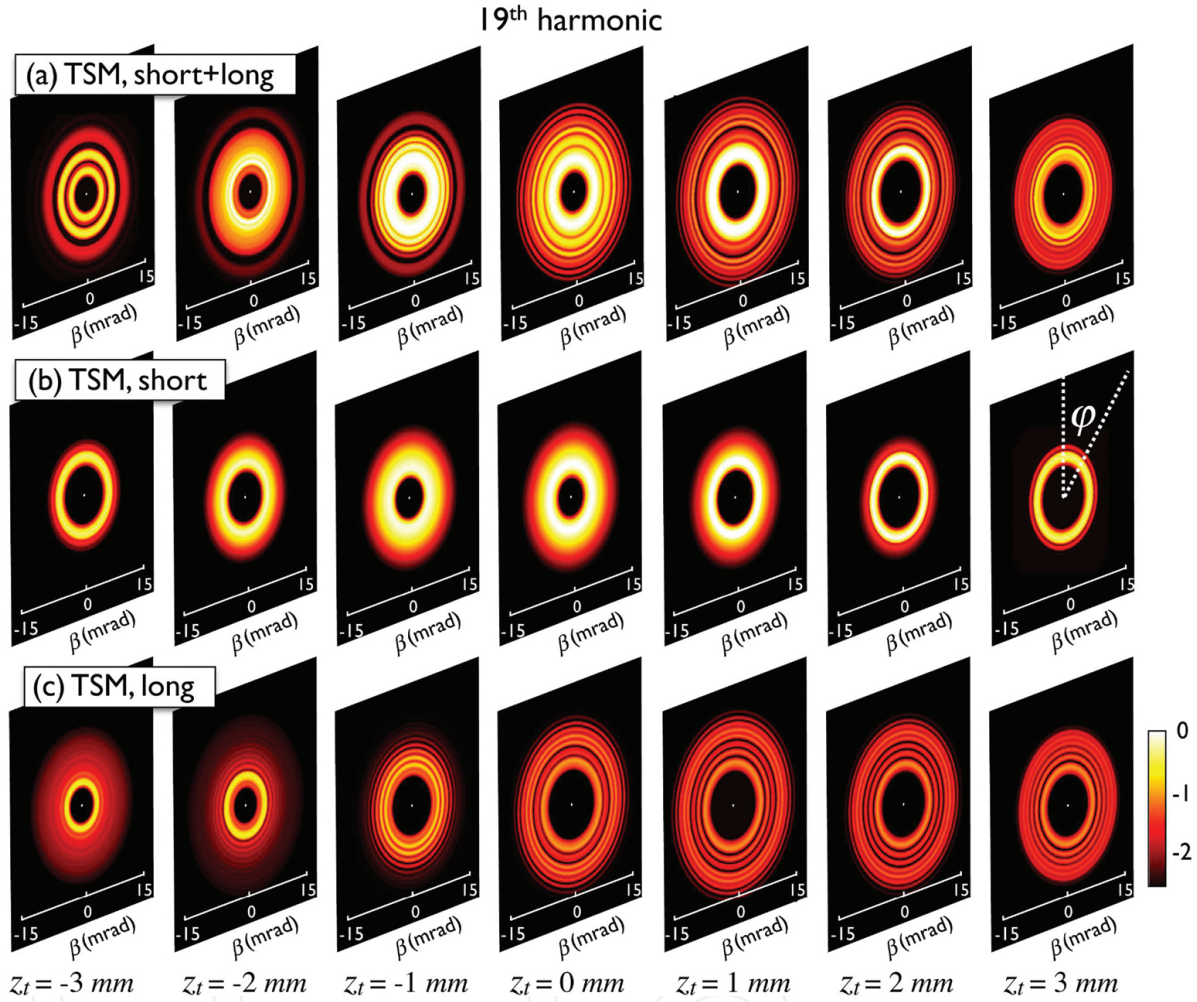

Figure 8. Far-field spatial intensity profile of the 19th harmonic for a slab placed at seven near-field positions, from $z_t = -3$ mm (left) to $z_t = 3$ mm (right), calculated with the TSM considering (a) short + long, (b) short, and (c) long quantum path contributions. Whereas short quantum path contributions exhibit similar intensity and structure independently of the near-field slab location, long ones are more intense if the slab is placed before the focus position. As a consequence, a rich vortex structure profile is obtained depending on the near-field slab position.

For better interpretation of the results that can be extracted from **Figure 7**, we represent in **Figure 8** the far-field divergence intensity profile of the 19th harmonic for seven slab positions z_t, from $z_t = -3$ mm to $z_t = 3$ mm, using the TSM and considering (a) short + long, (b) short, and (c) long quantum path contributions. From **Figures 7** and **8**, we observe that the emission dependence on the slab position is completely different for short and long quantum paths, being the short quantum path contribution the dominant, as expected from the shorter

excursion time [see Eq. (8)]. On the other hand, the intensity profile obtained from the short quantum path contributions is symmetric with z_t and that of the long ones is asymmetric, being more intense if $z_t < 0$. This behavior allows us to identify two different phase-matching regimes depending on the slab position with respect to the focus position. First, when the slab is placed before the focus ($z_t < 0$), long quantum paths are emitted with smaller divergence than the short ones. In fact, for $z_t = < -2$ mm, in **Figure 7(a)** and **(d)**, we can identify two well-separated contributions, with similar weight, corresponding to long quantum paths at low divergence and to short paths at higher divergence. This result becomes evident when analyzing the first column of **Figure 8**: two separated rings, from long (inner) and short (outer) quantum path contributions are obtained. Second, when the slab is placed after the focus position ($z_t > 0$), the short quantum path contributions dominate at smaller divergence angles while the long ones generate a less intense wriggle structure at large divergence angles.

As the results presented in **Figures 7** and **8** are performed for a thin slab, longitudinal phase-matching effects are neglected, and we can confirm that the behavior presented for different target positions is a direct consequence of transverse phase matching [28, 63]. Note that although in **Figure 7(a)** we have used an unrealistic 2D gas jet (1 μm -thick), when using a realistic 3D gas jet (500 μm-thick) the results are very similar [28].

4.2.2. Quantum path contributions in the 3D quantum SFA simulations: time-frequency analysis

In order to confirm the qualitative picture given by the TSM for the separation of short and long quantum paths, we perform a time-frequency analysis of the harmonic emission based on the 3D quantum SFA simulations using a realistic 500 μm thick 3D gas jet. The 3D quantum SFA model gives a full quantum description of the HHG emission but it does not provide an insight of the semiclassical picture in terms of quantum trajectories. However, with the help of the TFA, we can resolve the temporal order in which high-order harmonics are emitted, and thus, it allows us to extract relevant information about the quantum path contributions.

In the TFA of the harmonic emission [94], we select a spectral window in the harmonic spectrum and take its Fourier transform. By shifting the window to cover the entire harmonic spectrum, it is possible to resolve the time in which the different harmonics are generated. Nevertheless, due to the uncertainty principle, we have to be careful when interpreting the results of the TFA, as the width of the spectral window determines the resolution in time; the narrower the spectral window is, the less resolution we obtain in the temporal domain. The TFA has served to reveal unique features of HHG, like for example, the quantum path interferences due to multiple rescatterings in the HHG process [38, 95]. As it is usually observed in HHG calculations, the time evolution of the harmonic emission follows faithfully the distribution of rescattering energies of classical trajectories. As a consequence, from the TFA analysis, we can identify the short (long) quantum paths, as the TFA structures with positive (negative) slope, which give rise to a positive (negative) chirp in the harmonic emission, as commented in Section 2.2.

In **Figure 9**, we present the HHG spectra as a function of the divergence β for a 500 μm-thick gas jet placed 2 mm before (a) and after (b) the focus position, accordingly to the two regimes identified in **Figures 7** and **8**. As commented before, we observe that the harmonics exhibit similar divergence but their structure changes with the gas jet position. In the lower panels of **Figure 9**, we present the TFA of the HHG spectra emitted at different divergence β, where a Gaussian spectral window with FWHM $3\omega_0$ has been used to perform the TFA.

When the gas jet is placed before the focus (a), two ring structures can be identified, centered at divergences 3.5 and 6.2 mrad, whose TFA analysis are shown in panels (a1) and (a2), respectively. Whereas the TFA at 3.5 mrad (a1) presents structures with negative slope, at 6.2 mrad (a2), it presents structures with positive slope. As a consequence, long quantum paths are emitted with lower divergence and short ones with higher divergence, in agreement with the results previously obtained with the TSM in **Figures 7** and **8**. In addition, note that within each half-cycle, the long quantum path structures in (a1) are delayed in time with respect to the short ones in (a2), as expected from the semiclassical HHG theory [96].
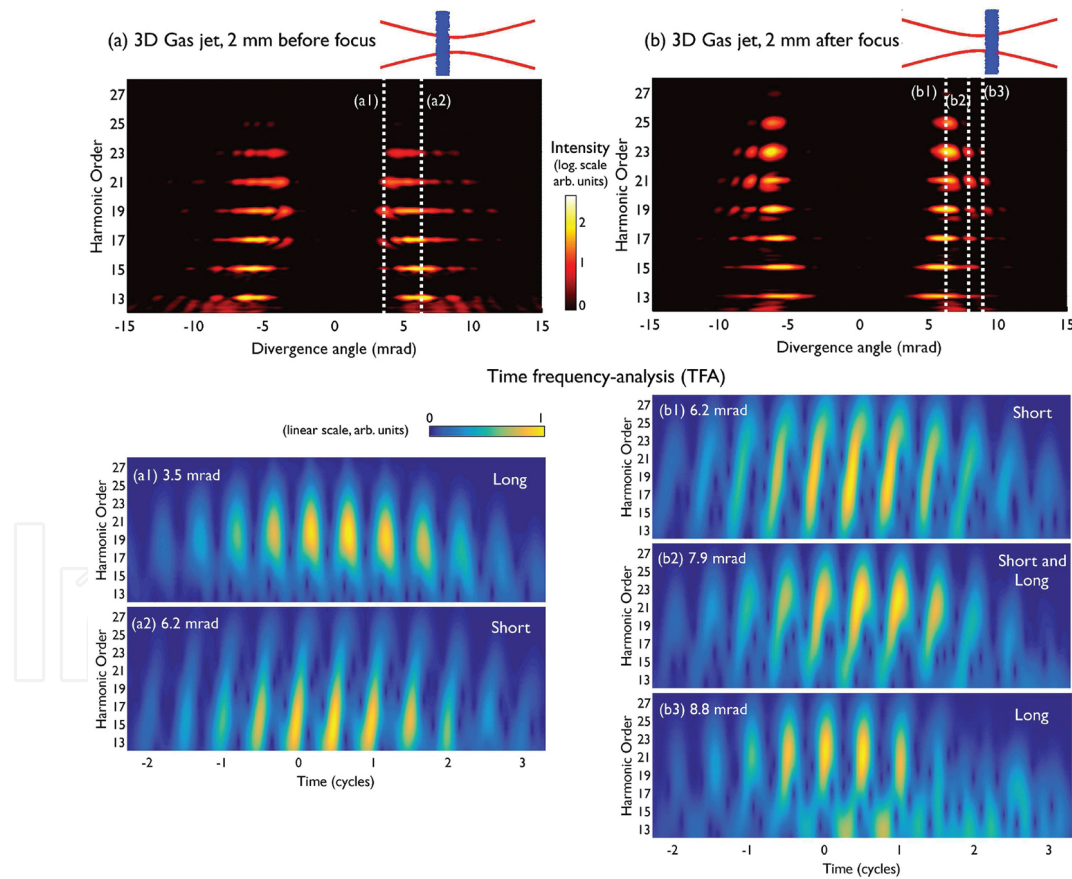

Figure 9. Time-frequency analysis based on the 3D quantum SFA model, for the XUV vortices generated in a 3D gas jet placed 2 mm before (a) and after (b) the focus position of the $LG_{1,0}$ beam. The top panels present the angular dependence of the harmonic radiation. The TFA of some particular angles (indicated by the dashed-white lines) are shown at the bottom panels, revealing the contribution of the short and long quantum paths, through the positive or negative slopes of the TFA structures, respectively.

On the other hand, when the gas jet is located after the focus (b), a prominent ring centered at 6.2 mrad and two secondary ones centered at 7.9 and 8.8 mrad are observed. The TFA analyses at those three divergences are shown in plots (b1) to (b3), respectively. We note that, in agreement with the TSM of **Figures 7** and **8**, (b1) is dominated by short quantum path contributions, whereas (b3) by long ones. Interestingly, the annular structure conformed around 7.9 mrad, (b2) presents contributions from both short and long quantum paths.

As a result, longitudinal phase matching, included through the 500 μm thickness of the gas jet, does not modify our previous conclusions in realistic gas jets, and thus the angular separation of highly-charged HHG vortices from different quantum paths is due to the transverse phase matching. In addition, this analysis through the TFA corroborates the adequacy of the TSM approach developed in Section 3.2. A rich scenario of XUV harmonic vortices is obtained, with different intensity structures and temporal properties due to the phase matching of short and long quantum path contributions. Note that long quantum path contributions are hard to observe experimentally due to their lower weight in the overall harmonic emission. Whereas with standard Gaussian beams, long paths have been successfully observed and characterized, the observation of XUV vortices obtained from long quantum path contributions remains unobserved.

4.3. Helical attosecond pulse trains

Finally, we proceed to study how the XUV vortices obtained from HHG are emitted in the temporal domain. As introduced in Section 2, one of the most exciting perspectives of HHG is the possibility of synthesizing XUV pulses of attosecond duration. For the correct synthesis, the spectrum should approximately satisfy two conditions: its structure should approach to that of a frequency comb, in which the harmonic intensities are similar, and the relative phase between the harmonics should be nearly constant. Fortunately, HHG satisfies these two conditions, and as XUV vortices are emitted with similar divergence in OAM-HHG, the radiation of several high-order harmonics can be synthesized to produce attosecond pulse trains.

In **Figure 10**, we present our simulation results of the temporal evolution of the high-order harmonics produced when the 500 μm-thick gas jet is centered at 2 mm after the focus position. Note that, at this position, short quantum path contributions dominate, and the HHG signal is maximized, as discussed in Section 4.2. We have filtered the low-order harmonics (below 11th) by simulating their transmission through an aluminum filter. First, in panel (a), we present five snapshots of the transverse intensity distribution of the integrated harmonic signal within half a cycle of the fundamental laser pulse, i.e., in a time interval of 1.33 fs. We observe that two well-defined intensity structures rotate in time, with a period of half a cycle.

In order to visualize the spatial structure of the HHG emission, we plot in panel (b) the spatiotemporal evolution of a given HHG intensity. We observe that a helical attosecond pulse train is obtained [27], i.e., an attosecond pulse train delayed along the azimuth φ according to the phase variation of the fundamental $LG_{1,0}$ beam. In the right part of panel (b), we show the attosecond pulse train obtained at four different azimuths ($\varphi=0$, $\pi/2$, π, and $3\pi/2$). Note that this particular spatiotemporal structure can also be identified as two interwinded helices that

result from the addition of harmonic vortices with different topological charges [97]. The number of interwinded helices is given by $\delta n \ell$, i.e., the order difference between successive harmonics in the spectrum (δn) times the topological charge of the driving beam (ℓ) [97]. In our case, $\ell = 1$ and $\delta n = 2$ as odd-order harmonics are produced, leading to two interwinded helices. As a consequence, the spatiotemporal structure of the helical attosecond beam can be sculpted by driving HHG with different topological charges (i.e., modifying ℓ) or wavelength combinations (and thus changing δn).
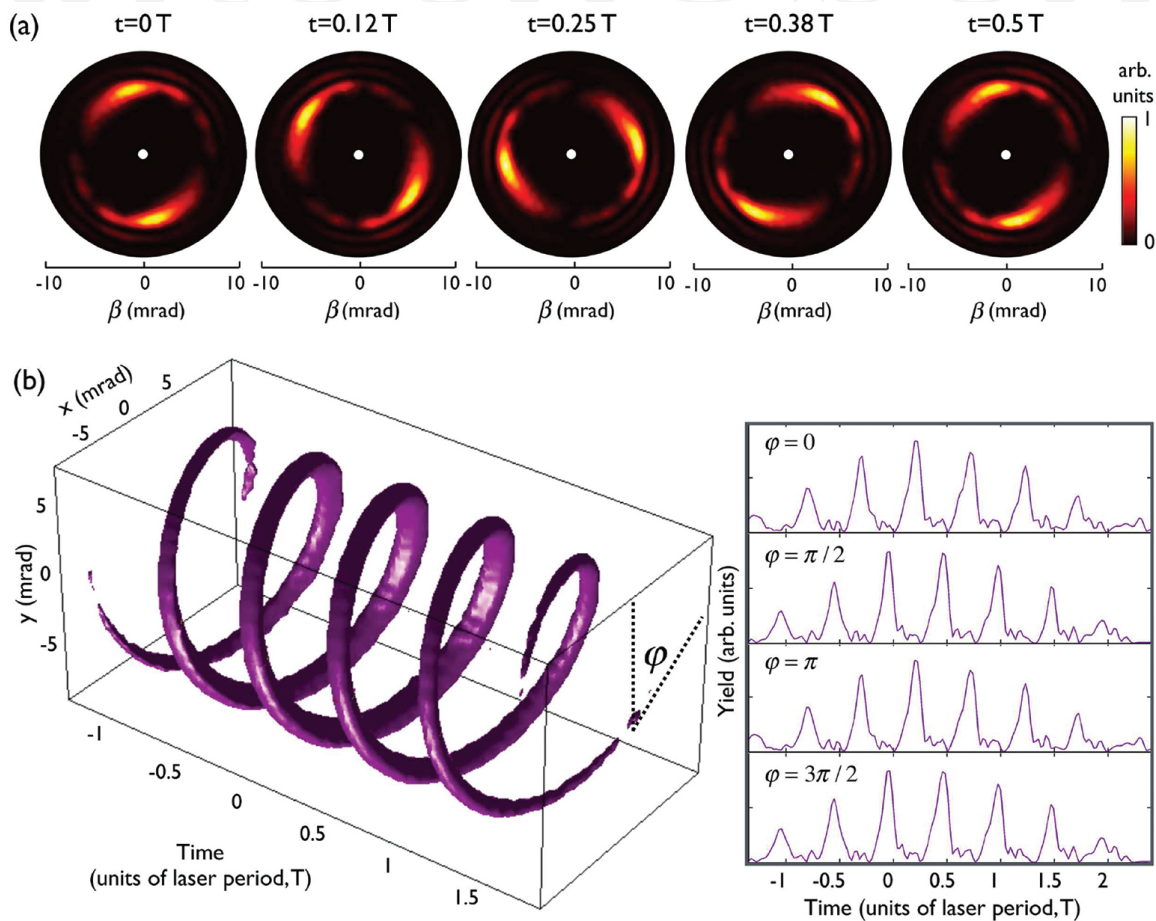

Figure 10. Attosecond helical beam structures of the emitted harmonic radiation obtained with the 3D quantum SFA model, for a 500 μm gas jet placed 2 mm after the focus position. In panel (a), we represent five snapshots of the trans-versal intensity structure at times equal to 0, 0.12, 0.25, 0.38, and 0.5 times the laser period (T), starting from the center of the IR pulse. We note that two well-defined intensity structures rotate in time, with a period of half a cycle. In panel (b), we represent the spatiotemporal structure of the XUV emission, exhibiting an helical attosecond beam composed of two interwinded helices. The right panels in (b) show the attosecond pulse train at four different azimuths ($\varphi = 0$, $\pi/2$, π, and $3\pi/2$). From this panel, we observe that the helical attosecond beam is composed by an attosecond pulse train that is delayed along the azimuthal coordinate.

The attosecond helical beams obtained from OAM-HHG were theoretically predicted in [27] and have been recently measured experimentally using the RABBITT technique [29]. Note that the carrier-envelope phase of the driving field is imprinted in the attosecond helical beam along

the azimuth. If the pulse duration of the driving field is restricted to few cycles, the number of pulses of the attosecond helical beam changes along the azimuthal direction, from an isolated pulse, to two pulses [27].

Finally, note that helical attosecond pulse trains with different divergence and chirp can be obtained by properly selecting the phase-matching properties to maximize the emission from short or long quantum path contributions [28]. Thus, our results show the possibility of generating helical attosecond pulse trains with different spatiotemporal structures that could be selected depending on the application. In these types of helical beams, which can also be generated using relativistic laser-matter interaction [23, 98], not only the phase but also the intensity profile possess a helical structure. As a consequence, these beams are able to exchange OAM in situations where standard Laguerre-Gauss beams cannot, opening an entirely new light-matter interaction regime [97].

5. Conclusions and outlook

Extreme ultraviolet OAM beams with high spatiotemporal coherence are now produced via HHG. When focusing an intense infrared OAM beam into a gas target, the HHG process combines the microscopic quantum mechanics with the macroscopic physics to imprint OAM into higher-order harmonics of the driving field. For instance, HHG maps the OAM properties of the driver into the harmonic vortices. When driven by pure vortices, the qth-order harmonic vortex is produced with topological charge $\ell_q = q\ell$ (ℓ being the topological charge of the driving vortex beam). In addition, the different harmonic vortices are emitted with similar divergence, thus allowing their synthesis into attosecond helical beams, unprecedented beams whose phase and intensity profiles exhibit a helical structure. Thus, the combination of the properties of OAM beams with the spatiotemporal characteristics of HHG opens an exciting perspective in ultrafast science.

Harmonic phase matching in the generation of XUV vortices allows for the selection of their spatiotemporal properties. Since beams carrying OAM have a very unique transverse structure, transverse phase matching plays a fundamental role in the macroscopic emission. With the help of a thin slab model, we unveil the role of different quantum path contributions in the generation of XUV vortices. For instance, the relative position between the gas jet and the beam focus allows for the spatial selection of XUV vortices produced from short and/or long quantum path contributions in the HHG process.

It has been recently shown that if OAM-HHG is driven by a combination of vortex beams with different topological charge, the generated XUV vortices exhibit a rich OAM content, arising from the nonperturbative behavior of HHG [30]. For instance, experimental methods to produce vortex beams with well-defined OAM may be imperfect, and such beams with several OAM contributions are naturally produced. Even when those imperfections are small, the sensibility of the nonperturbative nature of the HHG makes them visible. Another example where nonpure OAM beams are present is in the case of beams with fractional OAM, which

can be generated with spiral phase plates or spatial light modulators [99], or using conical refraction [100, 101].

In all these situations, the OAM dynamics are much more complex than those presented in this review. On the other hand, it has been recently shown that spin angular momentum can be transferred to the XUV harmonics in the HHG process [102], producing circularly polarized harmonics and attosecond pulses [87, 88, 103, 104]. New scenarios, in which orbital and spin angular momenta add a new degree of freedom to light-matter interaction, open an exciting route for the next generation of high-resolution, ultrafast, XUV/X-ray diagnostic tools for fundamental studies and applications.

6. Acknowledgements

Author details

Laura Rego[1], Julio San Román[1], Luis Plaja[1], Antonio Picón[2] and Carlos Hernández-García[1*]

*Address all correspondence to: carloshergar@usal.es

1 Grupo de Investigación en Aplicaciones del Láser y Fotónica, University of Salamanca, Salamanca, Spain

2 Argonne National Laboratory, Argonne, Illinois, USA

References

[1] L. Allen, M. W. Beijersbergen, R. J. C. Spreeuw, and J. P. Woerdman, Phys. Rev. A 45, 8185 (1992).

[2] M. S. Soskin and M. V. Vasnetsov, Progress Optics 42, 219–276 (2001).

[3] G.F. Calvo, A. Picón, and E. Bagan, Phys. Rev. A 73, 013805 (2006).

[4] J. Wang, J. Y. Yang, I. M. Fazal, N. Ahmed, Y. Yan, H. Huang, Y. Ren, Y. Yue, S. Dolinar, M. Tur, and A. E. Willner, Nat. Photon. 6, 488–496 (2012).

[5] X. Cai, J. Wang, M. J. Strain, B. Johnson-Morris, J. Zhu, M. Sorel, J. L. O'Brien, M. G. Thompson, and S. Yu, Science 338, 363 (2012).

[6] N. Simpson, L. Allen, and M. Padgett, J. of Mod. Opt. 43, 2485–2491 (1996).

[7] D. G. Grier, Nature 424, 810 (2003).

[8] S. Fürhapter, A. Jesacher, S. Bernet, and M. Ritsch-Marte, Opt. Lett. 30, 1953 (2005).

[9] A. Jesacher, S. Fürhapter, S. Bernet, and M. Ritsch-Marte, Phys. Rev. Lett. 94, 233902 (2005).

[10] J. P. Torres and L. Torner (Eds.), *Twisted Photons*. Wiley-VCH, Weinheim (2011).

[11] A. Sakdinawat and Y. Liu, Opt. Lett. 32, 2635 (2007).

[12] M. van Veenendaal and I. McNulty, Phys. Rev. Lett. 98, 157401 (2007).

[13] K.A. Nugent, Adv. Phys. 59, 1 (2010).

[14] A. Picón, J. Mompart, J. R. Vázquez de Aldana, L. Plaja, G. F. Calvo, and L. Roso, Opt. Exp. 18, 3660 (2010).

[15] A. Picón, A. Benseny, J. Mompart, J. R. Vázquez de Aldana, L. Plaja, G. F. Calvo, and L. Roso, New J. of Phys. 12, 083053 (2010).

[16] G. Gariepy, J. Leach, K. T. Kim, T. J. Hammond, E. Frumker, R. W. Boyd, and P. B. Corkum, Phys. Rev. Lett. 113, 153901 (2014).

[17] M. Z. Zürch, Optical vortices in the XUV chapter, in book *High-Resolution Extreme Ultraviolet Microscopy*. Springer Theses, Heidelberg (2015).

[18] A. G. Peele, P. J. McMahon, D. Paterson, C. Q. Tran, A. P. Mancuso, K. A. Nugent, J. P. Hayes, E. Harvey, B. Lai, and I. McNulty, Opt. Lett. 27, 1752 (2002).

[19] S. Sasaki and I. McNulty, Phys. Rev. Lett. 100, 124801 (2008).

[20] E. Hemsing, A. Marinelli, and J. B. Rosenzweig, Phys. Rev. Lett. 106, 164803 (2011).

[21] P. R. Ribič, D. Gauthier, and G. De Ninno, Phys. Rev. Lett. 112, 203602 (2014).

[22] E. Hemsing, G. Stupakov, D. Xiang, and A. Zholents, Rev. Mod. Phys. 86, 897 (2014).

[23] Y. Shi, B. Shen, L. Zhang, X. Zhang, W. Wang, and Z. Xu, Phys. Rev. Lett. 112, 235001 (2014).

[24] X. Zhang, B. Shen, Y. Shi, X. Wang, L. Zhang, W. Wang, J. Xu, L. Yi, and Z. Xu, Phys. Rev. Lett. 114, 173901 (2015).

[25] J. T. Mendonça and J. Viera, Phys. Plasmas 22, 123106 (2015).

[26] M. Zürch, C. Kern, P. Hansinger, A. Dreischuh, and Ch. Spielmann, Nat. Phys. 8, 743–746 (2012).

[27] C. Hernández-García, A. Picón, J. San Román, and L. Plaja, Phys. Rev. Lett. 111, 083602 (2013).

[28] C. Hernández-García, J. San Román, L. Plaja, and A. Picón, New J. Phys. 17, 093029 (2015).

[29] R. Géneaux, A. Camper, T. Auguste, O. Gobert, J. Caillat, R. Taeib, and T. Ruchon, Nat. Commun. 7, 12583 (2016).

[30] L. Rego, J. San Román, A. Picón, L. Plaja, and C. Hernández-García, "Nonperturbative Twist in the Generation of Extreme-Ultraviolet Vortex Beams", Phys. Rev. Lett. 117, 163202 (2016).

[31] T. Popmintchev, M. C. Chen, D. Popmintchev, P. Arpin, S. Brown, S. Ališauskas, G. Andriukaitis, T. Balčiunas, O. Mücke, A. Pugzlys, A. Baltuška, B. Shim, S. E. Schrauth, A. Gaeta, C. Hernández-García, L. Plaja, A. Becker, A. Jaron-Becker, M. M. Murnane, and H. C. Kapteyn, Science 336, 1287 (2012).

[32] D. Popmintchev, C. Hernández-García, F. Dollar, C. Mancuso, J. A. Pérez-Hernández, M. C. Chen, A. Hankla, X. Gao, B. Shim, A. L. Gaeta, M. Tarazkar, D. A. Romanov, R. J. Levis, J. A. Gaffney, M. Foord, S. B. Libby, A. Jaron-Becker, A. Becker, L. Plaja, M. M. Murnane, H. C. Kapteyn, and T. Popmintchev, Science 350, 1225 (2015).

[33] G. Farkas and C. Toth, Phys. Lett. A 168, 447 (1992).

[34] I. P. Christov, M. M. Murnane, and H. C. Kapteyn, Phys. Rev. Lett. 78, 1251–1254 (1997).

[35] P. M. Paul, E. S. Toma, P. Breger, G. Mullot, F. Augé, Ph. Balcou, H. G. Muller, and P. Agostini, Science 292, 1689 (2001).

[36] M. Hentschel, R. Kienberger, C. Spielmann, G. A. Reider, N. Milosevic, U. Heinzmann, M. Drescher, and F. Krausz, Nature 414, 509 (2001).

[37] E. Goulielmakis, M. Schultze, M. Hofstetter, V. S. Yakovlev, J. Gagnon, M. Uiberacker, A. L. Aquila, E. M. Gullikson, D. T. Attwood, R. Kienberger, F. Krausz, and U. Kleineberg, Science 320, 1614 (2008).

[38] C. Hernández-García, J. A. Pérez-Hernández, T. Popmintchev, M. M. Murnane, H. C. Kapteyn, A. Jaroń-Becker, A. Becker, and L. Plaja, Phys. Rev. Lett. 111, 033002 (2013).

[39] I. J. Sola, V. Collados, L. Plaja, C. Méndez, J. San Román, C. Ruiz, I. Arias, A. Villamarín, J. Atencia, M. Quintanilla, and L. Roso, Appl. Phys. B 91, 115 (2008).

[40] K. Yamane, Y. Toda, and R. Morita, Opt. Exp. 20, 18986 (2012).

[41] J. Atencia, M. V. Collados, M. Quintanilla, J. Marin-Saez, and I. J. Sola, Opt. Exp. 21, 21056–21061 (2013).

[42] A. L'Huillier, Ph. Balcou, S. Candel, K. J. Schafer, and K. C. Kulander, Phys. Rev. A 46, 2778 (1992).

[43] Th. Maiman, Nature 187, 493–494 (1960).

[44] P. A. Franken, A. E. Hill, C. W. Peters, and G. Weinreich, Phys. Rev. Lett. 7, 118–119 (1961).

[45] A. McPherson, G. Gibson, H. Jara, U. Johann, T. S. Luk, I. A. McIntyre, K. Boyer, and C. K. Rhode, J. Opt. Soc. Am. B 21, 595–601 (1987).

[46] M. Ferray, A. L'Huillier, X. F. Li, L. A. Lompré, G. Mainfray, and C. Manus, J. Phys. B: At. Mol. Opt. Phys. 21, L31–L35 (1988).

[47] P. B. Corkum, Phys. Rev. Lett. 71, 1994–1997 (1993).

[48] K. Schafer, B. Yang, L. F. DiMauro, and K. C. Kulander, Phys. Rev. Lett. 70, 1599–1602 (1993).

[49] P. Agostini and L. F. DiMauro, Rep. Prog. Phys. 67, 813–855 (2004).

[50] M. F. Kling and M. J. J. Vrakking, Annu. Rev. Phys. Chem. 59, 463–492 (2008).

[51] F. Krausz and M. Ivanov, Rev. Mod. Phys. 81, 163–234 (2009).

[52] M. Nisoli and G. Sansone, Prog. Quant. Electron. 33, 17–59 (2009).

[53] T. Popmintchev, M. Chen, P. Arpin, M. M. Murnane, and H. C. Kapteyn, Nat. Photon. 4, 822 (2010).

[54] L. Plaja, R. Torres, and A. Zaïr (Eds.), Attosecond Physics, Springer Series in Optical Sciences. Springer (Heidelberg, 2013).

[55] J. Miao, T. Ishikawa, I. K. Robinson, and M. M. Murnane, Science 348, 530 (2015).

[56] M. Lewenstein, P. Salieres, and A. L'Huillier, Phys. Rev. A 52, 4747 (1995).

[57] M. Bellini, C. Lynga, A. Tozzi, M. Gaarde, T. Hänsch, A. L'Huillier, and C. Wahlström, Phys. Rev. Lett. 81, 297–300 (1998).

[58] Y. Mairesse, A. de Bohan, L. J. Frasinski, H. Merdji, L. C. Dinu, P. Monchicourt, P. Breger, M. Kovacev, R. Taïeb, B. Carré, H. G. Muller, P. Agostini, and P. Saliéres, Science 302, 1540 (2003).

[59] J. Tate, T. Auguste, H. G. Muller, P. Salières, P. Agostini, and L. F. Di Mauro, *Scaling of Wave-Packet Dynamics in an Intense Midinfrared Field*. Phys. Rev. Lett. 98, 013901-1-4 (2007).

[60] D. D. Hickstein, P. Ranitovic, S. Witte, X. Tong, Y. Huismans, P. Arpin, X. Zhou, K. E. Keister, C. W. Hogle, B. Zhang, C. Ding, P. Johnsson, N. Toshima, M. J. J. Vrakking, M. M. Murnane, and H. C. Kapteyn, Phys. Rev. Lett. 109, 073004 (2012).

[61] A. Zaïr, M. Holler, A. Guandalini, F. Schapper, J. Biegert, L. Gallmann, U. Keller, A. S. Wyatt, A. Monmayrant, I. A. Walmsley, E. Cormier, T. Auguste, J. P. Caumes, and P. Salières, Phys. Rev. Lett. 100, 143902 (2008).

[62] M. B. Gaarde, J. L. Tate, and K. J. Schafer, J. Phys. B: At. Mol. Opt. Phys. 41, 132001 (2008).

[63] C. Hernández-García, I. J. Sola, and L. Plaja, Phys. Rev. A 88, 043848 (2013).

[64] P. Salières, A. L'Huillier, and M. Lewenstein, Phys. Rev. Lett. 74, 3776 (1995).

[65] P. Balcou, P. Salieres, A. L'Huillier, and M. Lewenstein, Phys. Rev. A, 55, 3204 (1997).

[66] T. Popmintchev, M. C. Chen, A. Bahabad, M. Gerrity, P. Sidorenko, O. Cohen, I. P. Christov, M. M. Murnane, and H. C. Kapteyn, Proc. Natl. Acad. Sci. USA 106, 10516 (2009).

[67] X. F. Li, A. L'Huillier, M. Ferray, L. A. Lompré, and G. Mainfray, Phys. Rev. A 39, 5751 (1989).

[68] J. L. Krause, K. J. Schafer, and K. C. Kulander, Phys. Rev. A 45, 4998 (1992).

[69] L. Lompré, A. L'Huillier, M. Ferray, P. Monot, G. Mainfray, and C. Manus, J. Opt. Soc. Am. B 7, 754–761 (1990).

[70] J. Seres, P. Wobrauschek, C. Streli, V. S. Yakovlev, E. Seres, F. Krausz, and C. Spielmann, New J. Phys. 8, 251–251 (2006).

[71] J. A. Pérez-Hernández, L. Roso, and L. Plaja, Opt. Exp. 17, 9891 (2009).

[72] K. Zhao, Q. Zhang, M. Chini, Y. Wu, X. Wang, and Z. Chang, Opt. Lett. 37, 3891 (2012).

[73] M. C. Chen, C. Mancuso, C. Hernández-García, F. Dollar, B. Galloway, D. Popmintchev, P. C. Huang, B. Walker, L. Plaja, A. A. Jaron-Becker, A. Becker, M. M. Murnane, H. C. Kapteyn, and T. Popmintchev, Proc. Natl. Acad. Sci. USA 111, E2361–E2367 (2014).

[74] S. M. Teichmann, F. Silva, S. L. Cousin, M. Hemmer, and J. Biegert, Nat. Comm. 7, 11493 (2016).

[75] M. Lewenstein, Ph. Balcou, M. Yu. Ivanov, A. L'Huillier, and P. B. Corkum, Phys. Rev. A 49, 2117 (1994).

[76] K. Varjú, Y. Mairesse, B. Carré, M. B. Gaarde, P. Johnsson, S. Kazamias, R. López-Martens, J. Mauritsson, K. J. Schafer, Ph. Balcou, A. L'Huillier, and P. Saliéres, J. of Mod. Opt. 52, 379–394 (2005).

[77] C. Hernández-García and L. Plaja, J. of Phys. B 45, 074021 (2012).

[78] C. Hernández-García, J. A. Pérez-Hernández, J. Ramos, E. Conejero Jarque, L. Roso, and L. Plaja, Phys. Rev. A 82, 022432 (2010).

[79] C. Hernández-García, T. Popmintchev, H. C. Kapteyn, M. M. Murnane, L. Plaja, A. Becker, and A. Jaron-Becker, New J. Phys. 18, 073031 (2016).

[80] L. V. Keldysh, Zh. Eksp. Teor. Fiz. 47, 1945 (1964) [Sov. Phys. JETP 20, 1307 (1965)].

[81] F. H. M. Faisal, J. Phys. B 6, L89 (1973).

[82] H. R. Reiss, Phys. Rev. A 22, 1786 (1980).

[83] W. Becker, A. Lohr, M. Kleber, and M. Lewenstein, Phys. Rev. A 56, 645 (1997).

[84] J. A. Pérez-Hernández, C. Hernández-García, J. Ramos, E. Conejero, L. Plaja, and L. Roso, New Methods For Computing High-Order Harmonic Generation and Propagation, Springer Series in Chemical Physics Vol. 100 (Springer, New York, 2011), Chap. 7, p. 145.

[85] C. Hernández-García, W. Holgado, L. Plaja, B. Alonso, F. Silva, M. Miranda, H. Crespo, and I. J. Sola, Opt. Exp. 16, 21497–21508 (2015).

[86] M. Kretschmar, C. Hernández-García, D. S. Steingrube, L. Plaja, U. Morgner, and M. Kovacev, Phys. Rev. A 88, 013805 (2013).

[87] T. Fan, P. Grychtol, R. Knut, C. Hernández-García, D. D. Hickstein, D. Zusin, C. Gentry, F. J. Dollar, C. A. Mancuso, C. W. Hogle, O. Kfir, D. Legut, K. Carva, J. L. Ellis, K. M. Dorney, C. Chen, O. G. Shpyrko, E. E. Fullerton, O. Cohen, P. M. Oppeneer, D. B. Milosevic, A. Becker, A. A. Jaron-Becker, T. Popmintchev, M. M. Murnane, and H. C. Kapteyn, Proc. Natl. Acad. Sci. USA 112, 14206 (2015).

[88] D. D. Hickstein, F. J. Dollar, P. Grychtol, J. L. Ellis, R. Knut, C. Hernández-García, C. Gentry, D. Zusin, J. M. Shaw, T. Fan, K. M. Dorney, A. Becker, A. Jaroń-Becker, H. C. Kapteyn, M. M. Murnane, and Ch. G. Durfee, Nat. Photon. 9, 743 (2015).

[89] I. V. Basistiy, V. Yu. Bazhenov, M. S. Soskin, and M. V. Vasnetsov, Opt. Comm. 103, 422–428 (1993).

[90] K. Dholakia, N. B. Simpson, M. J. Padgett, and L. Allen, Phys. Rev. A. 54, R3742 (1996).

[91] J. Courtial, K. Dholakia, L. Allen, and M. J. Padgett, Phys. Rev. A. 56, 4193 (1997).

[92] A. Berzanskis, A. Matijosius, A. Piskarskas, V. Smilgevicius, and A. Stabinis, Opt. Comm. 140, 273–276 (1997).

[93] A.S. Ostrovsky, C. Rickenstorff-Parrao, and V. Arrizón, Opt. Lett. 38, 534 (2013).

[94] P. Antoine, B. Piraux, and A. Maquet, Phys. Rev. A 51, R1750 (1995).

[95] C. Hernández-García and L. Plaja, Phys. Rev. A 93, 023402 (2016).

[96] P. Antoine, A. L'Huillier, and M. Lewenstein, Phys. Rev. Lett. 77, 1234–1237 (1996).

[97] G. Pariente and F. Quéré, Opt. Lett. 40, 2037–40 (2015).

[98] J. Leach, E. Yao, and M. J. Padgett, New J. Phys. 6, 71 (2004).

[99] A. Turpin, Yu. V. Loiko, A. Peinado, A. Lizana, T. K. Kalkandjiev, J. Campos, and J. Mompart, Opt. Exp. 23, 5704–5715 (2015).

[100] K. E. Ballantine, J. F. Donegan, and P. R. Eastham, Sci. Adv. 2, e1501748 (2016).

[101] Zs. Lécz and A. Andreev, Phys. Rev. E 93, 013207 (2016).

[102] A. Fleischer, O. Kfir, T. Diskin, P. Sidorenko, and O. Cohen, Nat. Photon. 8, 543 (2014).

[103] C. Chen, Z. Tao, C. Hernández-García, P. Matyba, A. Carr, R. Knut, O. Kfir, D. Zusin, C. Gentry, P. Grychtol, O. Cohen, L. Plaja, A. Becker, A. Jaron-Becker, H. Kapteyn, and M. Murnane, Sci. Adv. 2, e1501333 (2016).

[104] C. Hernández-García, C. G. Durfee, D. D. Hickstein, T. Popmintchev, A. Meier, M. M. Murnane, H. C. Kapteyn, I. J. Sola, A. Jaron-Becker, and A. Becker, Phys. Rev. A 93, 043855 (2016).